Acta Cryst C STRUCTURAL CHEMISTRY

ISSN 2053-2296

YK-4-250, a synthetic telmisartan–tempol conjugate: crystal structure of a stabilized free radical containing an angiotensin AT_1 receptor inhibitor

Simon Friedrich,[a]‡ Yali Kong,[b]‡ Faik N. Musayev,[c] Milton L. Brown[d]* and B. Frank Gupton[e]

[a]Department of Chemical and Life Science Engineering, Virginia Commonwealth University, Richmond, VA 23220, USA, [b]Department of Biomedical and Translational Sciences, Macon & Joan Brock Virginia Health Sciences at Old Dominion University, Norfolk, VA 23507, USA, [c]Department of Medicinal Chemistry, School of Pharmacy, Virginia Commonwealth University, Richmond, VA 23298, USA, [d]Department of Medicine, Macon & Joan Brock Virginia Health Sciences at Old Dominion University, Norfolk, VA 23501, USA, and [e]Medicines for All Institute, Virginia Commonwealth University, Richmond, VA 23284, USA. *Correspondence e-mail: brownml@odu.edu

Received 8 April 2026
Accepted 14 July 2026

Edited by A. G. Oliver, University of Notre Dame, USA

‡ These authors contributed equally to this work

Keywords: angiotensin receptor blocker; ARB; radiation mitigator; crystal structure; solid-state characterization; radical stabilization.

CCDC reference: 2522559

Supporting information: this article has supporting information at journals.iucr.org/c

We report the first crystal structure of the telmisartan–tempol conjugate 2,2,6,6-tetramethyl-1-(λ′-oxidaneyl)piperidin-4-yl 4′-[(1,7′-dimethyl-2′-propyl-1*H*,3′*H*-[2,5′-bibenzo[*d*]imidazol]-3′-yl)methyl]-[1,1′-biphenyl]-2-carboxylate free radical (YK-4-250, $C_{42}H_{46}N_5O_3$), a dual-function inhibitor designed to target both the angiotensin II type 1 receptor (AT_1R) and reactive oxygen species (ROS). Structural analysis reveals a unique crystal architecture in which the nitroxide radical is stabilized within a sterically protected environment while preserving the telmisartan pharmacophore essential for high-affinity receptor antagonism. YK-4-250 is a novel small-molecule conjugate of telmisartan and tempol that incorporates a catalytic stabilized nitroxide radical and was rationally designed to mitigate gastrointestinal acute radiation syndrome (GI-ARS).

1. Introduction

The development of a small-molecule mitigator for radiation-induced tissue injury remains a significant unmet need in both clinical and national defense applications. High-dose exposure to ionizing radiation from radiological accidents or nuclear detonations triggers complex multi-organ pathologies. While the hematopoietic system is highly vulnerable, exposure to higher doses ranging from 6 to 10 Gy induces gastrointestinal acute radiation syndrome (GI-ARS) (Freeman, 2025). The lethal pathology of GI-ARS manifests rapidly, driven by the profound ablation of highly proliferative intestinal epithelial stem cells (IESCs) within the crypts of Lieberkühn, coupled with severe microvascular endothelial damage (Paris *et al.*, 2001; Shaker & Rubin, 2010). This mucosal barrier breakdown leads to structural villus blunting, severe diarrhea, systemic sepsis, and death, typically benchmarked within 10 to 30 days in a partial-body irradiation (PBI) LD50/30 model (Kumar *et al.*, 2026). While medical countermeasures exist to support bone marrow recovery (Bunin *et al.*, 2023), there remains a critical therapeutic void for orally available small-molecule countermeasures capable of mitigating GI-ARS when administered 24 h or longer post-exposure.

A mounting body of evidence highlights a lethal synergistic feed-forward loop between the local renin–angiotensin system (RAS) and chronic oxidative stress in driving this radiation-

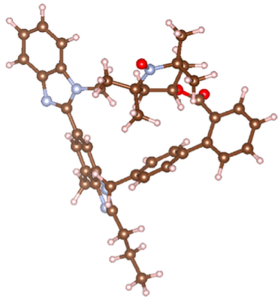

induced tissue injury (Kumar *et al.*, 2024; DiCarlo *et al.*, 2025). Ionizing radiation initiates immediate radiolytic water cleavage, generating a massive burst of primary reactive oxygen species (ROS). However, the long-term propagation of tissue damage is sustained by chronic metabolic ROS production. This sustained oxidative stress is largely mediated by the upregulation of Angiotensin II (Ang II) and its subsequent binding to the Angiotensin II Type 1 receptor (AT_1R) (Fan *et al.*, 2023).

Activation of the AT_1R by Ang II triggers the membrane-bound enzyme complex NADPH oxidase (Nox), dramatically amplifying intracellular superoxide ($O_2^{\bullet-}$) generation (Garrido *et al.*, 2009). This secondary wave of ROS induces persistent mitochondrial dysfunction, lipid peroxidation of endothelial membranes, and pro-inflammatory signalling *via* nuclear factor kappa beta (NFkb). In the gastrointestinal tract, this cascade accelerates endothelial cell apoptosis, deprives the intestinal crypts of necessary perfusion, and halts crypt regeneration (Orzechowska-Licari *et al.*, 2022). Conversely, elevated ROS levels further upregulate local AT_1R expression (Bhatt *et al.*, 2014) and stimulate local Ang II production (Dikalov & Nazarewicz, 2013), locking the irradiated GI microenvironment into a chronic cycle of inflammation, vasoconstriction, and fibroproliferative remodeling (Nguyen Dinh Cat *et al.*, 2013). To intercept this destructive signalling loop, YK-4-250 was rationally designed as a synthetic conjugate of telmisartan, a clinically approved AT_1R antagonist, and tempol, a stable nitroxide radical with well-established antioxidant and radioprotective properties (Kumar *et al.*, 2026). The compound blocks radiation-induced Ang II signalling at the AT_1R while simultaneously scavenging ROS generated by radiolysis of water and activation of NADPH oxidase (Nox).

The physiological rationale for this specific hybrid design exploits critical mechanistic synergies to achieve what monotherapy cannot. By blocking the AT_1R, the telmisartan core prevents the initial Ang II-dependent assembly and activation of Nox, cutting off the primary enzymatic source of secondary metabolic ROS. Concurrently, the integrated nitroxide tempol moiety acts as a highly efficient intracellular superoxide dismutase (SOD) mimetic and peroxynitrite scavenger, rapidly detoxifying residual $O_2^{\bullet-}$ and preventing the formation of highly destructive hydroxyl radicals (Wilcox, 2010). This dual mechanism simultaneously relieves AT_1R-mediated microvascular vasoconstriction and protects the thin-walled endothelial cells of the villi from oxidative apoptosis, thereby preserving the sub-epithelial vascular niche essential for regenerating intestinal stem cells (Kumar *et al.*, 2026). Furthermore, telmisartan offers a distinct pharmacological of extended half-life of nearly 22 hours, which works in tandem to extend the half-life of tempol's antioxidant property to downregulate pro-inflammatory cytokines (TNF-a, IL-1b) and dampen the systemic inflammatory response accompanying barrier breakdown.

Crucially, this bifunctional strategy addresses the severe pharmacokinetic limitations that have historically hindered free antioxidants from clinical translation. While native antioxidant proteins or free nitroxides suffer from poor oral bioavailability and ultra-short biological half-lives, the lipophilic telmisartan core serves as an effective pharmacological vehicle. This scaffold optimizes gastrointestinal absorption and tissue distribution, yielding the first orally available small-molecule mitigator engineered to break the AT_1R–ROS feed-forward loop directly within the injured mesenteric and intestinal mucosa after exposure to partial body irradiation (PBI) LD50/30. The integration of these two pharmacophores, AT_1R antagonism and catalytic antioxidation, represents a dual-mechanism strategy for mitigating GI-ARS. Here, we report the first single-crystal X-ray structure of a telmisartan–tempol conjugate, providing structural insight into its molecular geometry, radical-stabilizing interactions, and conformational features that may underlie its biological activity and support its development as a potential active pharmaceutical ingredient (API) for GI-ARS.

2. Experimental

2.1. Synthesis and crystallization

YK-4-250 was synthesized by the coupling of telmisartan and tempol under EDCI/HOBt coupling conditions in DMF at room temperature for 12 h. The product was purified by normal-phase flash chromatography using methylene chloride–methanol as eluent to give analytically pure material in 78% yield (Fig. 1). Structure characterization was performed by HRMS (TOF): calculated for $C_{42}H_{47}N_5O_3$ $(M + H)^+$: 669.3679; found: 669.3675. Single crystals suitable for X-ray diffraction

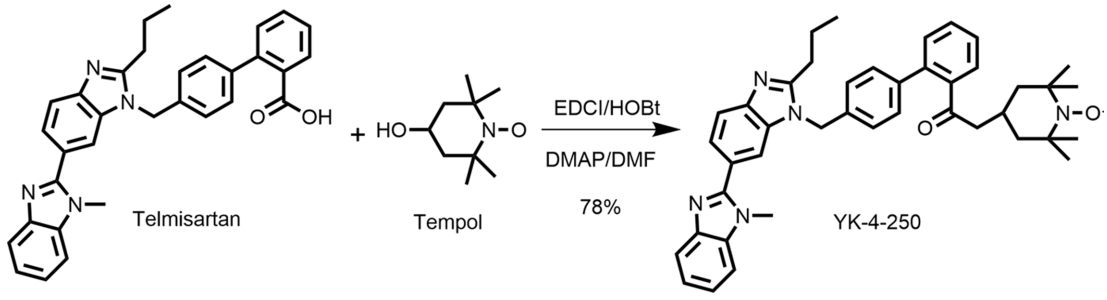

Figure 1
The reaction scheme for the preparation of YK-4-250.

were obtained by slow evaporation of a 1:1 (*v*/*v*) ethyl acetate/hexanes solution over 7 d at room temperature.

2.2. Refinement

Crystal data, data collection and structure refinement details are summarized in Table 1. H atoms bonded to C atoms were placed in calculated positions and refined using a riding model, with U_{iso}(H) = 1.2U_{eq}(C) for aromatic/methylene groups and 1.2U_{eq}(C) for methyl groups. The C—H bond distances were set to *de facto* standard values corresponding to their respective hybridization states.

Table 1
Experimental details.

Crystal data	
Chemical formula	$C_{42}H_{46}N_5O_3$
M_r	668.84
Crystal system, space group	Monoclinic, *Ia*
Temperature (K)	295
a, *b*, *c* (Å)	9.4556 (1), 27.1981 (3), 15.0100 (2)
β (°)	106.828 (2)
V (Å^3)	3694.89 (8)
Z	4
Radiation type	Cu $K\alpha$
μ (mm^{-1})	0.60
Crystal size (mm)	0.65 × 0.38 × 0.20
Data collection	
Diffractometer	Rigaku XtaLAB AFC11
Absorption correction	Multi-scan (*CrysAlis PRO*; Rigaku OD, 2021)
T_{min}, T_{max}	0.550, 1.000
No. of measured, independent and observed [$I > 2\sigma(I)$] reflections	16498, 4987, 4906
R_{int}	0.019
(sin $\theta/\lambda)_{max}$ (Å^{-1})	0.627
Refinement	
$R[F^2 > 2\sigma(F^2)]$, $wR(F^2)$, S	0.029, 0.082, 1.06
No. of reflections	4987
No. of parameters	459
No. of restraints	2
H-atom treatment	H-atom parameters constrained
$\Delta\rho_{max}$, $\Delta\rho_{min}$ (e Å^{-3})	0.12, −0.11
Absolute structure	Flack *x* determined using 1302 quotients $[(I^+) - (I^-)]/[(I^+) + (I^-)]$ (Parsons *et al.*, 2013)
Absolute structure parameter	0.06 (11)

Computer programs: *CrysAlis PRO* (Rigaku OD, 2021), *SHELXT* (Sheldrick, 2015*a*), *SHELXL2016* (Sheldrick, 2015*b*), and *OLEX2* (Dolomanov *et al.*, 2009).

2.3. Simultaneous differential scanning calorimetry (DSC)/thermogravimetric analysis (TGA)

Differential scanning calorimetry (DSC) is widely regarded as a key technique for inferring the thermodynamic relationships between multiple crystal forms (Yu, 1995). Simultaneous DSC/TGA (SDT) was performed on an SDT650 to supplement the obtained DSC data with any mass change events. A single ∼2.5 mg crystal of YK-4-250 was added to an aluminium DSC pan without a sealing lid. The chamber was held inert by steady N_2 gas purge while the chamber was ramped to 471.15 K at a rate of 5 K min^{-1}. Three cycles were programmed to cool to 388.15 K and subsequently heated to 471.15 K; this was done to capture any melting and fusion events and verify these events' parameters. However, none were observed, a single exothermic event (70.3 J g^{-1}) was observed at an onset of 446.75 K with a peak at 453.15 K. This event was accompanied by a 0.2% weight loss (Fig. 2). It is hypothesized that the melting of the compound frees the radical and triggers an irreversible decomposition. Due to this, it was not possible to determine the thermodynamic stability of this structure or if other more thermodynamically stable conformations exist by DSC. Telmisartan is known to exhibit two polymorphs; therefore, it is pertinent to elucidate if this

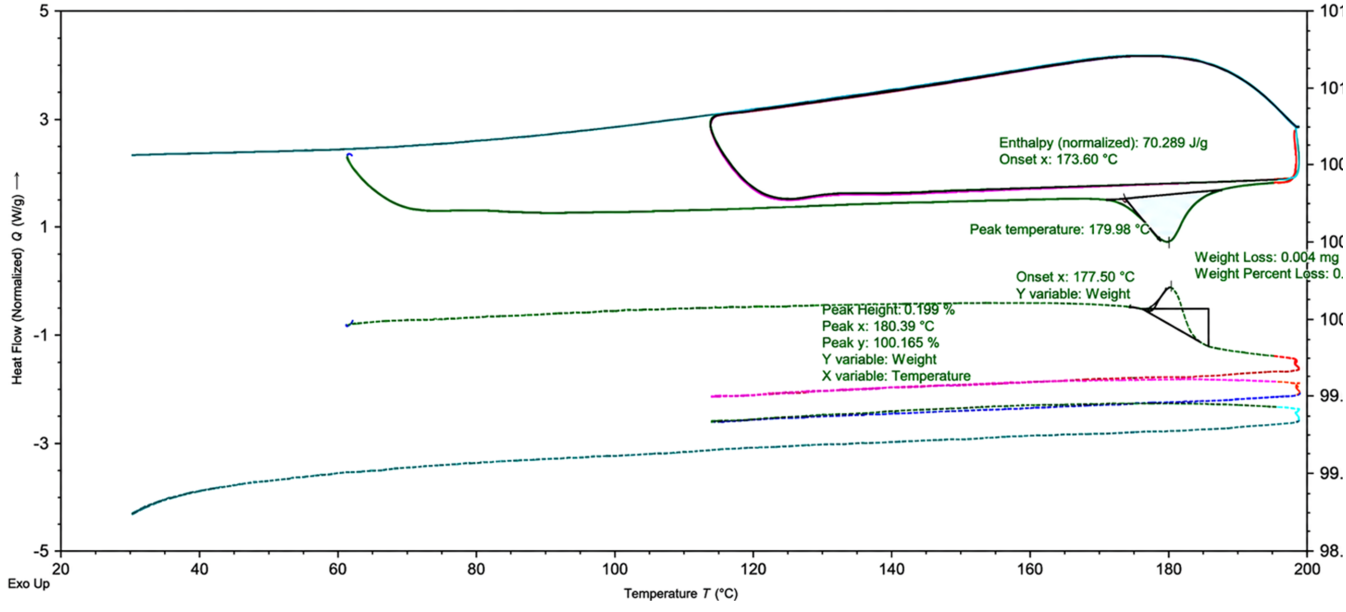

Figure 2
(Top) DSC trace of three cycles 388.15–471.15 K and (bottom) TGA curve of three cycles 388.15–471.15 K.

compound also exhibits polymorphism in future work (Cunha *et al.*, 2021; Dinnebier *et al.*, 2000).

2.4. *ORCA* density functional theory (DFT) optimization of a single molecule

The theoretical single-molecule structure was pre-optimized with XTB (Dinnebier *et al.*, 2000) set to normal and fully optimized with *ORCA* (Version 6.0.1) using the B3LYP functional and def2-SVP basis set using TightSCF convergence; the radical is specified *via* one unpaired electron designation (Neese, 2022; Bannwarth *et al.*, 2019).

3. Results

3.1. Structural commentary and DFT theoretical structure

YK-4-250 crystallizes in the monoclinic space group *Ia* with one molecule in the asymmetric unit. The molecule adopts an extended conformation in which the telmisartan and tempol fragments are oriented nearly perpendicular to each other.

Key bond lengths and angles in the telmisartan-derived biphenyl fragments match those in previously reported telmisartan structures; however, the dibenzimidazole interfacial angle of YK-4-250 [Fig. 3(*a*)] is significantly more eclipsed than in telmisartan form A (Amano *et al.*, 2012; Cunha *et al.*, 2021; Dinnebier *et al.*, 2000; Singh *et al.*, 2024). The presence of the radical does not significantly distort the tempol backbone. The interfacial angles of the experimentally calculated conformer's biphenyl rings and dibenzimidazole system are listed and compared to the theoretically optimized single molecule, as well as the known telmisartan form A in (see Table S1 in the supporting information) (Dinnebier *et al.*, 2000). The theoretical single-molecule structure [Fig. 3(*b*)] revealed that the radical is 94% confined to the nitroxide moiety, as calculated *via* total spin occupancy in the N—O system.

The comparison of the experimentally obtained crystal structure to the optimized single-molecule structure provides insight into the influence of crystal packing on molecular conformation. The radical confinement to the nitroxide moiety is not meaningfully affected by the crystal structure, in both the gas-optimized single molecule and crystal structure, 94% of the radical electron spin is confined to the N—O moiety. The dihedral (interfacial) angles of the ring systems in the molecule give insight into the intermolecular interactions and intramolecular conformation. The dihedral angle changes of the dibenzimidazole and biphenyl rings reflects the balance between intermolecular interactions and intramolecular conjugation. Biphenyl by itself in solution at room temperature exhibits a rather flexible dihedral angle in the range 32–45° (Eaton & Steele, 1973). The DFT-optimized single molecule exhibits a comparable interfacial angle of 47.3°, whereas the packed crystal shows a significant shift to 61.3°. Furthermore, the close intermolecular contact distance falls well within the sum of the respective atomic van der Waals radii, confirming that the observed packing is stabilized by standard van der Waals forces. For the dibenzimidazole rings, no exact analogue was found in the literature. However, an article by Antonov and co-workers described the dihedral angles of a 2′-phenyl-2,5′-bibenzodimidazole [2,5′-BBIm (c1)] to be 18.28° in the aqueous phase (Antonov *et al.*, 2022). For comparison, the DFT-optimized single molecule exhibits an interfacial angle of 37.9°, whereas the experimentally obtained crystal structure displays a reduced angle of 31.9°. This contraction in the solid state is likely driven by fewer intermolecular interactions involving the benzimidazole subunits.

3.2. Supramolecular features

In the extended lattice, molecules pack in layers parallel to the *ab* plane (see Fig. S2 in the supporting information).

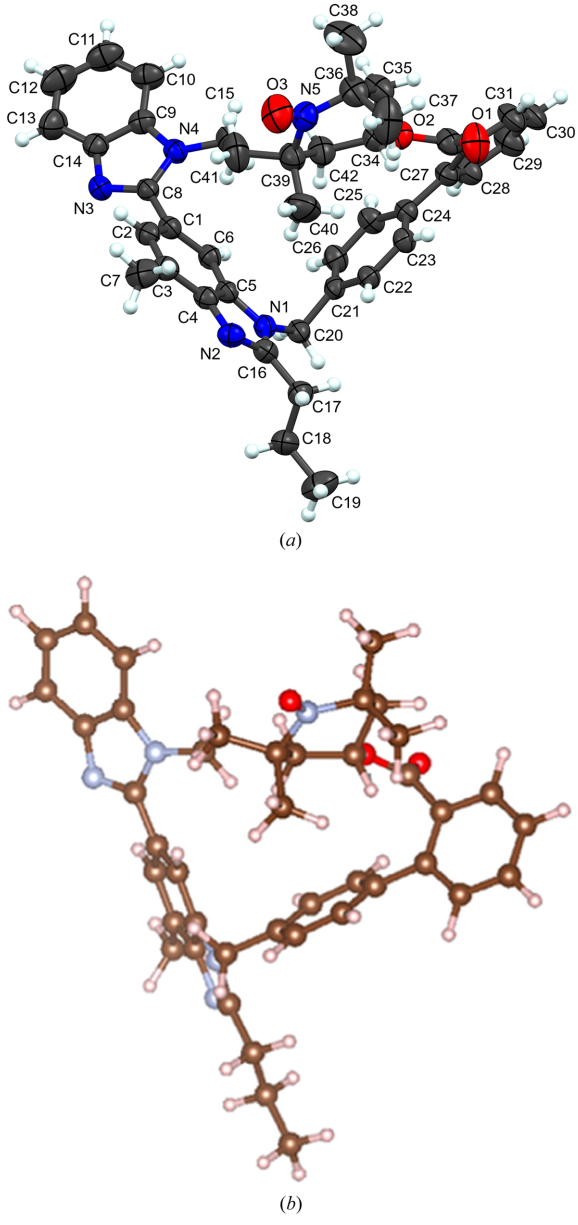

Figure 3
(*a*) Experimentally measured YK-4-250, drawn with 50% probability displacement ellipsoids, and (*b*) theoretically calculated YK-4-250 *via ORCA*.

Table 2
List of the nearest 12 H-atom neighbors of the radical O atom.

The H atoms belonging to the dimethyl sub-units adjacent to the N—O moiety are marked in bold. Angles are included for O3···H—C.

Atom pair	Distance (Å)	Angle (°)
O3···H41*A*	**2.45**	**96.50**
O3···H38*C*	**2.53**	**92.80**
O3···H15*B*	2.53	158.03
O3···H40*C*	**2.63**	**99.00**
O3···H37*A*	**2.65**	**98.20**
O3···H29	2.76	155.42
O3···H38*A*	**2.88**	**72.40**
O3···H10	2.92	161.74
O3···H41*C*	**2.97**	**68.30**
O3···H37*C*	**3.29**	**60.40**
O3···H40*A*	**3.30**	**60.00**
O3···H15*C*	3.65	70.06

Intermolecular C—H···O contacts (3.1 Å) link molecules into one-dimensional chains along the *b* axis. Additional stabilization is provided by three C—H···π interactions (Table 3) involving the phenyl and benzimidazole rings. The crystal structure exhibits mainly van der Waals interactions. The nitroxide radical does not participate in significant intermolecular interactions, consistent with preserved radical stability in the solid state. In fact, the only near neighbors (<4 Å) are methyl or phenyl H atoms (Table 2) for the nearest 12 H-atom neighbors of the radical O atom.

3.3. Database survey

A search of the Cambridge Structural Database (CSD, Version 5.46; Groom *et al.*, 2016) revealed no previously reported crystal structures of telmisartan–tempol conjugates or related stabilized nitroxide–AT_1R inhibitor analogues. While crystal forms of telmisartan (Dinnebier *et al.*, 2000) and structural analogues of tempol (Cunha *et al.*, 2021) have been described independently, to our knowledge, YK-4-250 represents the first structurally characterized molecule in which an AT_1R antagonist is covalently linked to a stable nitroxide radical.

4. Discussion

4.1. Radical stabilization through crystal packing

The most significant finding is the structure by which the nitroxide radical in YK-4-250 is stabilized in the solid state. Unlike tempol derivatives (Cunha *et al.*, 2021), which typically rely on hydrogen-bonding networks involving the nitroxide O atom, YK-4-250 presents no conventional hydrogen-bond donors; both benzimidazole N atoms are substituted and no O—H or N—H groups are present, structurally precluding the participation of atom O3 in such interactions. Strong hydrogen-bond donors would impose a thermodynamic driving force sufficient to position donors near O3 despite steric cost; their absence means the steric environment provided by the flanking dimethyl substituents becomes the sole determinant of access to the radical center. The result is a sterically protected environment in which only the adjacent CH_3 groups and aromatic H atoms from neighboring YK-4-250 molecules approach within 4 Å of O3, exclusively as weak C—H···O contacts (Table 2). This intramolecular steric shielding, which restricts intermolecular access to the radical center rather than relying on conventional hydrogen bonding, may offer a promising design principle for developing stable radical-containing pharmaceuticals that must preserve their paramagnetic character during storage and formulation. B3LYP/def2-SVP spin population analysis in *ORCA* (Version 6.0.1) confirms 94% spin confinement to the N—O moiety, with negligible change between the gas-phase optimized and crystal-conformation geometries, indicating that radical localization is robust to the conformational constraints imposed by crystal packing.

Table 3
List of the C—H···*Cg* (*Cg* is a ring centroid) distances and the corresponding C—H···*Cg* angles.

*Cg*1 is the centroid of the N3/C8/N4/C9/C14 ring, *Cg*2 that of the C21–C26 ring, and *Cg*3 that of the C1–C6 ring.

C—H···*Cg*	Distance (Å)	Angle (°)
C13—H13···*Cg*1	2.90	164.40
C2—H2···*Cg*2	2.98	158.84
C41—H41B···*Cg*3	2.99	171.64

4.2. Crystal packing and solid-state organization

Unlike telmisartan form A, which achieves crystal cohesion through extensive hydrogen bonding (Cunha *et al.*, 2021), YK-4-250 organizes its solid-state structure through a hierarchy of weaker interactions. At the primary level, intermolecular C—H···O contacts (H···O = 3.1 Å) link molecules into one-dimensional chains along the *b* axis, with these chains assembling into layers parallel to the *ab* plane. Three C—H···π interactions involving the phenyl and benzimidazole ring systems (Table 2) provide lateral cohesion between chains. Together these contacts define a packing arrangement in which directional weak interactions substitute collectively for the conventional hydrogen-bonding networks present in related structures.

4.3. Thermal behaviour and polymorph considerations

Thermal analysis revealed a single exothermic event at 446.75 K accompanied by minimal mass loss (0.2%). This behavior renders conventional DSC-based polymorph screening unfeasible, leaving the question of whether additional thermodynamically stable forms exist. Given that telmisartan exhibits two known polymorphs (Dinnebier *et al.*, 2000) and the flexible ester linker at the tempol conjugation site introduces additional degrees of freedom, polymorph screening through solution-mediated approaches remains necessary to inform solid-form control during pharmaceutical development. Identifying the most stable polymorph and understanding transformation pathways will be critical for ensuring consistent manufacturing, long-term stability of this potential drug candidate, and FDA evaluation.

4.4. Implications for structure–activity optimization and formulation development

The crystal structure provides a key insight for designing next-generation derivatives that balance receptor-binding potency with radical stabilization. Key design considerations include: (i) maintaining the conformation that preserves the active AT_1R pharmacophore geometry, (ii) engineering intramolecular interactions that stabilize the radical through spatial isolation, and (iii) minimizing intermolecular contacts with the nitroxide center that could compromise radical stability during processing or storage. The characterization of the solid-state properties of YK-4-250, including its packing behavior and thermal stability profile, informs formulation strategies for this promising radiation mitigator and supports the continued development as a dual-mechanism pharmaceutical agent for gastrointestinal acute radiation syndrome.

Acknowledgements

Special thanks are extended to the Prudence and Louis Ryan Endowed Chair of Research for support to MLB. The funders played no role in the study design, data collection, analysis, and interpretation of data, or the writing of this article. The authors acknowledge support from the Medicines for All Institute and the Virginia Health Sciences research programs. We thank the VCU X-ray Crystallography Core Facility for instrument access and technical assistance. This work was supported in part by an NIH/NIAID grant.

Conflict of interest

MLB and YK are inventors on patents describing YK-4-250 (US20120196896A1; US17/728,485), licensed to Trocar Pharmaceuticals Inc. *via* Georgetown University.

Funding information

Funding for this research was provided by: National Institutes of Health, National Institute of Allergy and Infectious Diseases (grant No. 1U01AI187033-01 to M. L. Brown).

References

Amano, Y., Yamaguchi, T., Ohno, K., Niimi, T., Orita, M., Sakashita, H. & Takeuchi, M. (2012). *Hypertens. Res.* **35**, 715–719.
Antonov, L., Kawauchi, S. & Shirata, K. (2022). *Molecules* **27**, 1064.
Bannwarth, C., Ehlert, S. & Grimme, S. (2019). *J. Chem. Theory Comput.* **15**, 1652–1671.
Bhatt, S. R., Lokhandwala, M. F. & Banday, A. A. (2014). *Clin. Exp. Hypertens.* **36**, 367–373.
Bunin, D. I., Javitz, H. S., Gahagen, J., Bakke, J., Lane, J. H., Andrews, D. A. & Chang, P. Y. (2023). *Int. J. Radiat. Oncol. Biol. Phys.* **117**, 705–717.
Cunha, A. C., Ferreira, V. F., Vaz, M. G. F., Cassaro, R. A. A., Resende, J. A. L. C., Sacramento, C. Q., Costa, J., Abrantes, J. L., Souza, T. M. L. & Jordão, A. K. (2021). *Mol. Divers.* **25**, 2035–2043.
DiCarlo, A., Button, J., Cassatt, D., Chang, A., Finklea, L., Iyer, N., Moroni, M., Rios, C., Rudokas, M., Satyamitra, M., Taliaferro, L., Winters, T. & Homer, M. (2025). *Disaster Med. Publ. Heal. Prep.* **19**, e199.
Dikalov, S. I. & Nazarewicz, R. R. (2013). *Antioxid. Redox Signal.* **19**, 1085–1094.
Dinnebier, R. E., Sieger, P., Nar, H., Shankland, K. & David, W. I. (2000). *J. Pharm. Sci.* **89**, 1465–1479.
Dolomanov, O. V., Bourhis, L. J., Gildea, R. J., Howard, J. A. K. & Puschmann, H. (2009). *J. Appl. Cryst.* **42**, 339–341.
Eaton, V. J. & Steele, D. (1973). *J. Chem. Soc. Faraday Trans. 2* **69**, 1601–1608.
Fan, J. F., Wang, Y. K., Liu, M., Liu, G. S., Min, T. J., Chen, R. Y. & He, Y. (2023). *Sci. Rep.* **13**, 11659.
Freeman, M. L. (2025). *Cell Death Discov.* **11**, 235.
Garrido, A. M. & Griendling, K. K. (2009). *Mol. Cell. Endocrinol.* **302**, 148–158.
Groom, C. R., Bruno, I. J., Lightfoot, M. P. & Ward, S. C. (2016). *Acta Cryst.* B**72**, 171–179.
Kumar, V. P., Kong, Y., Dolland, R., Brown, S. R., Wang, K., Dolland, D., Mu, D. & Brown, M. L. (2024). *Antioxidants* **13**, 1207.
Kumar, V. P., Kong, Y., Wang, K., Britton-Jenkins, A., Dulan, S., Moore, L., Saunders, D., May, R., Towner, R., Ghosh, S., Houchen, C. & Brown, M. (2026). *Sci. Rep.* https://doi.org/10.1038/s41598-026-53734-7.
Neese, F. (2022). *WIREs Comput. Mol. Sci.* **12**, e1606.
Nguyen Dinh Cat, A., Montezano, A. C., Burger, D. & Touyz, R. M. (2013). *Antioxid. Redox Signal.* **19**, 1110–1120.
Orzechowska-Licari, E. J., LaComb, J. F., Giarrizzo, M., Yang, V. W. & Bialkowska, A. B. (2022). *J. Vis. Exp.* **185**, e64028.
Paris, F., Fuks, Z., Kang, A., Capodieci, P., Juan, G., Ehleiter, D., Haimovitz-Friedman, A., Cordon-Cardo, C. & Kolesnick, R. (2001). *Science* **293**, 293–297.
Parsons, S., Flack, H. D. & Wagner, T. (2013). *Acta Cryst.* B**69**, 249–259.
Rigaku OD (2021). *CrysAlis PRO*. Rigaku Corporation, Tokyo, Japan.
Shaker, A. & Rubin, D. C. (2010). *Transl. Res.* **156**, 180–187.
Sheldrick, G. M. (2015*a*). *Acta Cryst.* A**71**, 3–8.
Sheldrick, G. M. (2015*b*). *Acta Cryst.* C**71**, 3–8.
Singh, M., Murugan, N. A., Kongsted, J., Zhan, P., Banerjee, U. C. & Poongavanam, V. (2024). *Cryst. Growth Des.* **24**, 6354–6363.
Wilcox, C. S. (2010). *Pharmacol. Ther.* **126**, 119–145.
Yu, L. (1995). *J. Pharm. Sci.* **84**, 966–974.

supporting information

Acta Cryst. (2026). C**82**, 547-552 [https://doi.org/10.1107/S2053229626007242]

YK-4-250, a synthetic telmisartan–tempol conjugate: crystal structure of a stabilized free radical containing an angiotensin AT_1 receptor inhibitor

Simon Friedrich, Yali Kong, Faik N. Musayev, Milton L. Brown and B. Frank Gupton

Computing details

2,2,6,6-Tetramethyl-1-(λ′-oxidaneyl)piperidin-4-yl 4′-[(1,7′-dimethyl-2′-propyl-1*H*,3′*H*-[2,5′-bibenzo[*d*]imidazol]-3′-yl)methyl]-[1,1′-biphenyl]-2-carboxylate

Crystal data

$C_{42}H_{46}N_5O_3$
M_r = 668.84
Monoclinic, *Ia*
a = 9.4556 (1) Å
b = 27.1981 (3) Å
c = 15.0100 (2) Å
β = 106.828 (2)°
V = 3694.89 (8) Å^3
Z = 4
F(000) = 1428
D_x = 1.202 Mg m^{-3}
Melting point: 450.65 K
Cu *Kα* radiation, *λ* = 1.54184 Å
Cell parameters from 13399 reflections
θ = 3.2–74.7°
μ = 0.60 mm^{-1}
T = 295 K
Prism, clear light orange
0.65 × 0.38 × 0.20 mm

Data collection

Rigaku XtaLAB AFC11 diffractometer
Radiation source: Rotating-anode X-ray tube, Rigaku (Cu) X-ray Source
Mirror monochromator
Detector resolution: 13.3333 pixels mm^{-1}
ω scans
Absorption correction: multi-scan (CrysAlis PRO; Rigaku OD, 2021)
T_{min} = 0.550, T_{max} = 1.000
16498 measured reflections
4987 independent reflections
4906 reflections with $I > 2\sigma(I)$
R_{int} = 0.019
θ_{max} = 75.1°, θ_{min} = 3.3°
h = −7→11
k = −23→33
l = −18→18

Refinement

Refinement on F^2
Least-squares matrix: full
$R[F^2 > 2\sigma(F^2)]$ = 0.029
$wR(F^2)$ = 0.082
S = 1.06
4987 reflections
459 parameters
2 restraints
Primary atom site location: dual
Hydrogen site location: inferred from neighbouring sites
H-atom parameters constrained
$w = 1/[\sigma^2(F_o^2) + (0.0543P)^2 + 0.4013P]$ where $P = (F_o^2 + 2F_c^2)/3$
$(\Delta/\sigma)_{max}$ = 0.001
$\Delta\rho_{max}$ = 0.12 e Å^{-3}
$\Delta\rho_{min}$ = −0.11 e Å^{-3}
Extinction correction: SHELXL2016 (Sheldrick, 2015*b*), $Fc^*=kFc[1+0.001xFc^2\lambda^3/\sin(2\theta)]^{-1/4}$
Extinction coefficient: 0.00309 (16)
Absolute structure: Flack *x* determined using 1302 quotients [(I+)-(I-)]/[(I+)+(I-)] (Parsons *et al.*, 2013)
Absolute structure parameter: 0.06 (11)

Special details

Geometry. All esds (except the esd in the dihedral angle between two l.s. planes) are estimated using the full covariance matrix. The cell esds are taken into account individually in the estimation of esds in distances, angles and torsion angles; correlations between esds in cell parameters are only used when they are defined by crystal symmetry. An approximate (isotropic) treatment of cell esds is used for estimating esds involving l.s. planes.

Fractional atomic coordinates and isotropic or equivalent isotropic displacement parameters (Å²)

	x	*y*	*z*	U_{iso}*/U_{eq}
O2	0.74960 (16)	0.76214 (5)	0.42813 (9)	0.0532 (3)
N3	0.13509 (19)	0.53006 (6)	0.37466 (11)	0.0515 (4)
N1	0.73645 (17)	0.56316 (5)	0.64019 (10)	0.0428 (3)
N2	0.6376 (2)	0.58611 (6)	0.75260 (11)	0.0494 (4)
N4	0.26340 (18)	0.58488 (6)	0.31727 (10)	0.0460 (3)
O1	0.9339 (2)	0.81552 (6)	0.48660 (14)	0.0797 (5)
O3	0.3505 (2)	0.81083 (8)	0.61658 (14)	0.0852 (5)
N5	0.4382 (2)	0.79978 (7)	0.56816 (12)	0.0573 (4)
C33	0.8820 (2)	0.78187 (7)	0.43573 (15)	0.0533 (4)
C5	0.5863 (2)	0.56727 (6)	0.59801 (12)	0.0409 (3)
C8	0.2493 (2)	0.55951 (6)	0.39351 (12)	0.0417 (4)
C24	0.9204 (2)	0.66983 (6)	0.41545 (12)	0.0420 (4)
C21	0.86352 (19)	0.59403 (6)	0.52836 (12)	0.0403 (3)
C4	0.5259 (2)	0.58142 (7)	0.66917 (12)	0.0440 (4)
C3	0.3732 (2)	0.58809 (7)	0.65026 (12)	0.0490 (4)
C16	0.7599 (2)	0.57517 (7)	0.73277 (12)	0.0458 (4)
C32	0.9565 (2)	0.75868 (7)	0.37063 (13)	0.0488 (4)
C22	0.9155 (2)	0.63948 (6)	0.56598 (12)	0.0422 (4)
H22	0.930400	0.645032	0.629169	0.051*
C26	0.8371 (2)	0.58723 (7)	0.43347 (13)	0.0489 (4)
H26	0.800917	0.557219	0.406737	0.059*
C25	0.8643 (2)	0.62482 (7)	0.37781 (12)	0.0497 (4)
H25	0.844464	0.619693	0.314111	0.060*
C1	0.3509 (2)	0.56697 (6)	0.48817 (12)	0.0428 (4)
C20	0.8437 (2)	0.55203 (6)	0.58980 (13)	0.0446 (4)
H20A	0.811298	0.523070	0.551619	0.054*
H20B	0.938197	0.544514	0.634284	0.054*
C2	0.2878 (2)	0.58051 (7)	0.55918 (13)	0.0468 (4)
H2	0.185904	0.584453	0.544417	0.056*
C9	0.1447 (2)	0.57061 (7)	0.24327 (13)	0.0474 (4)
C23	0.9455 (2)	0.67659 (6)	0.51131 (12)	0.0430 (4)
H23	0.982710	0.706421	0.538444	0.052*
C6	0.5017 (2)	0.55970 (6)	0.50660 (12)	0.0436 (4)
H6	0.543869	0.550290	0.460415	0.052*
C14	0.0671 (2)	0.53651 (7)	0.27999 (14)	0.0509 (4)
C27	0.9643 (2)	0.70802 (7)	0.35700 (12)	0.0443 (4)
C17	0.9088 (2)	0.57289 (7)	0.80253 (13)	0.0525 (4)
H17A	0.906729	0.591762	0.856971	0.063*
H17B	0.980363	0.588105	0.776162	0.063*

C18	0.9591 (3)	0.52068 (9)	0.83263 (17)	0.0647 (6)
H18A	0.887117	0.505436	0.858647	0.078*
H18B	0.961409	0.501873	0.778162	0.078*
C28	1.0290 (3)	0.69221 (8)	0.28963 (15)	0.0575 (5)
H28	1.033147	0.658672	0.278549	0.069*
C34	0.6760 (2)	0.77726 (7)	0.49660 (14)	0.0506 (4)
H34	0.748813	0.780890	0.557765	0.061*
C36	0.5170 (3)	0.84149 (8)	0.54089 (16)	0.0626 (5)
C39	0.4861 (3)	0.74726 (8)	0.57285 (16)	0.0610 (5)
C31	1.0217 (3)	0.79105 (8)	0.32236 (17)	0.0656 (6)
H31	1.021941	0.824564	0.334655	0.079*
C15	0.3740 (3)	0.62120 (10)	0.31379 (17)	0.0680 (6)
H15A	0.392234	0.642258	0.367249	0.102*
H15B	0.338978	0.640511	0.258204	0.102*
H15C	0.463889	0.604867	0.313600	0.102*
C19	1.1084 (3)	0.51810 (13)	0.90306 (18)	0.0830 (8)
H19A	1.180542	0.532863	0.877747	0.125*
H19B	1.134047	0.484345	0.918189	0.125*
H19C	1.105999	0.535452	0.958311	0.125*
C10	0.0965 (3)	0.58631 (9)	0.15094 (14)	0.0641 (6)
H10	0.148101	0.609647	0.127423	0.077*
C35	0.5935 (3)	0.82486 (8)	0.46881 (16)	0.0619 (5)
H35A	0.520020	0.820666	0.408984	0.074*
H35B	0.662016	0.850148	0.462087	0.074*
C29	1.0873 (3)	0.72469 (9)	0.23865 (16)	0.0666 (6)
H29	1.126902	0.713145	0.192683	0.080*
C7	0.3070 (3)	0.60404 (11)	0.72578 (16)	0.0715 (7)
H7A	0.327025	0.579622	0.774005	0.107*
H7B	0.202127	0.607850	0.700041	0.107*
H7C	0.349761	0.634818	0.751374	0.107*
C13	−0.0621 (3)	0.51568 (9)	0.22368 (18)	0.0732 (7)
H13	−0.115056	0.492790	0.247142	0.088*
C42	0.5678 (3)	0.73715 (8)	0.50012 (17)	0.0601 (5)
H42A	0.620371	0.706190	0.514598	0.072*
H42B	0.496215	0.733987	0.439322	0.072*
C30	1.0859 (3)	0.77418 (9)	0.25669 (18)	0.0697 (6)
H30	1.128335	0.796264	0.224618	0.084*
C12	−0.1090 (4)	0.53016 (12)	0.1317 (2)	0.0852 (9)
H12	−0.193886	0.516194	0.092167	0.102*
C11	−0.0320 (3)	0.56520 (12)	0.09669 (17)	0.0786 (8)
H11	−0.068399	0.574663	0.034705	0.094*
C38	0.4020 (5)	0.88081 (12)	0.4974 (3)	0.1059 (12)
H38A	0.323739	0.866323	0.448834	0.159*
H38B	0.447751	0.906563	0.471841	0.159*
H38C	0.362226	0.894209	0.544264	0.159*
C41	0.3461 (4)	0.71577 (12)	0.5504 (3)	0.0926 (9)
H41A	0.295273	0.721447	0.596332	0.139*
H41B	0.372491	0.681664	0.550885	0.139*

H41C	0.282848	0.724433	0.490034	0.139*
C37	0.6297 (4)	0.86185 (14)	0.6286 (2)	0.0987 (10)
H37A	0.579949	0.870549	0.673790	0.148*
H37B	0.676624	0.890455	0.612623	0.148*
H37C	0.702995	0.837239	0.654273	0.148*
C40	0.5826 (4)	0.73558 (15)	0.6711 (2)	0.0970 (10)
H40A	0.672508	0.754194	0.684087	0.146*
H40B	0.605372	0.701106	0.675797	0.146*
H40C	0.530544	0.744077	0.715157	0.146*

Atomic displacement parameters (Å²)

	U^{11}	U^{22}	U^{33}	U^{12}	U^{13}	U^{23}
O2	0.0539 (8)	0.0505 (7)	0.0616 (8)	0.0051 (6)	0.0269 (6)	−0.0076 (6)
N3	0.0491 (9)	0.0478 (8)	0.0563 (8)	−0.0056 (7)	0.0132 (7)	0.0089 (6)
N1	0.0418 (8)	0.0444 (7)	0.0449 (7)	−0.0011 (6)	0.0169 (6)	0.0026 (6)
N2	0.0560 (9)	0.0517 (8)	0.0416 (7)	0.0053 (7)	0.0159 (7)	0.0017 (6)
N4	0.0481 (8)	0.0472 (8)	0.0461 (7)	−0.0015 (7)	0.0189 (7)	0.0035 (6)
O1	0.0843 (12)	0.0672 (10)	0.1010 (12)	−0.0194 (9)	0.0481 (10)	−0.0338 (9)
O3	0.0823 (12)	0.0996 (14)	0.0949 (12)	0.0062 (10)	0.0593 (10)	−0.0101 (10)
N5	0.0529 (10)	0.0676 (10)	0.0585 (9)	0.0033 (8)	0.0273 (8)	−0.0051 (8)
C33	0.0609 (12)	0.0417 (9)	0.0636 (11)	0.0029 (8)	0.0280 (9)	−0.0003 (8)
C5	0.0435 (9)	0.0388 (8)	0.0439 (8)	0.0010 (7)	0.0183 (7)	0.0040 (6)
C8	0.0418 (9)	0.0406 (8)	0.0455 (8)	0.0023 (7)	0.0168 (7)	0.0057 (6)
C24	0.0447 (9)	0.0395 (8)	0.0461 (8)	0.0038 (7)	0.0201 (7)	0.0015 (6)
C21	0.0347 (8)	0.0407 (8)	0.0488 (8)	0.0012 (7)	0.0174 (7)	0.0011 (6)
C4	0.0497 (10)	0.0432 (8)	0.0438 (8)	0.0053 (7)	0.0207 (8)	0.0047 (6)
C3	0.0546 (11)	0.0510 (10)	0.0476 (9)	0.0121 (8)	0.0246 (8)	0.0052 (7)
C16	0.0523 (10)	0.0421 (8)	0.0437 (8)	−0.0007 (7)	0.0150 (8)	0.0032 (7)
C32	0.0536 (11)	0.0428 (8)	0.0553 (9)	0.0063 (8)	0.0245 (8)	0.0058 (7)
C22	0.0450 (9)	0.0424 (8)	0.0414 (8)	−0.0007 (7)	0.0159 (7)	0.0003 (6)
C26	0.0584 (11)	0.0398 (8)	0.0516 (9)	−0.0070 (8)	0.0210 (9)	−0.0064 (7)
C25	0.0624 (12)	0.0466 (9)	0.0431 (8)	−0.0029 (8)	0.0201 (8)	−0.0032 (7)
C1	0.0461 (10)	0.0396 (8)	0.0454 (8)	0.0005 (7)	0.0177 (7)	0.0039 (6)
C20	0.0432 (9)	0.0394 (8)	0.0555 (9)	0.0037 (7)	0.0212 (8)	0.0046 (7)
C2	0.0447 (9)	0.0489 (9)	0.0518 (9)	0.0091 (7)	0.0218 (8)	0.0075 (7)
C9	0.0490 (10)	0.0496 (9)	0.0449 (8)	0.0080 (8)	0.0156 (8)	−0.0028 (7)
C23	0.0475 (9)	0.0374 (7)	0.0464 (8)	−0.0019 (7)	0.0171 (7)	−0.0032 (6)
C6	0.0456 (9)	0.0456 (8)	0.0449 (8)	−0.0008 (7)	0.0211 (7)	0.0016 (7)
C14	0.0496 (10)	0.0437 (9)	0.0569 (10)	0.0028 (8)	0.0115 (8)	0.0006 (7)
C27	0.0478 (10)	0.0425 (8)	0.0474 (8)	0.0047 (7)	0.0214 (7)	0.0041 (7)
C17	0.0536 (11)	0.0528 (10)	0.0486 (9)	−0.0040 (9)	0.0107 (8)	0.0015 (8)
C18	0.0595 (13)	0.0612 (12)	0.0668 (12)	−0.0013 (10)	0.0078 (10)	0.0154 (10)
C28	0.0729 (14)	0.0487 (10)	0.0632 (11)	0.0095 (10)	0.0388 (10)	0.0058 (8)
C34	0.0551 (11)	0.0492 (10)	0.0533 (9)	0.0053 (8)	0.0248 (9)	−0.0030 (7)
C36	0.0732 (14)	0.0522 (10)	0.0757 (13)	0.0078 (10)	0.0424 (12)	−0.0054 (9)
C39	0.0592 (12)	0.0607 (12)	0.0690 (12)	0.0001 (10)	0.0278 (10)	0.0077 (10)
C31	0.0830 (16)	0.0425 (10)	0.0837 (14)	0.0059 (10)	0.0436 (13)	0.0153 (10)

C15	0.0641 (14)	0.0753 (14)	0.0664 (12)	−0.0177 (11)	0.0216 (11)	0.0185 (11)
C19	0.0668 (16)	0.110 (2)	0.0664 (13)	0.0268 (16)	0.0092 (12)	0.0032 (14)
C10	0.0741 (15)	0.0745 (14)	0.0457 (10)	0.0116 (11)	0.0207 (10)	0.0023 (9)
C35	0.0776 (15)	0.0497 (10)	0.0716 (12)	0.0132 (10)	0.0426 (12)	0.0048 (9)
C29	0.0825 (17)	0.0673 (13)	0.0679 (12)	0.0121 (12)	0.0499 (13)	0.0112 (10)
C7	0.0689 (15)	0.0975 (18)	0.0580 (11)	0.0299 (13)	0.0340 (11)	0.0033 (11)
C13	0.0646 (15)	0.0642 (13)	0.0803 (15)	−0.0113 (11)	0.0042 (12)	−0.0053 (11)
C42	0.0610 (13)	0.0490 (10)	0.0755 (13)	0.0026 (9)	0.0280 (11)	−0.0030 (9)
C30	0.0841 (17)	0.0589 (12)	0.0818 (14)	0.0087 (12)	0.0488 (13)	0.0237 (11)
C12	0.0769 (18)	0.0924 (19)	0.0680 (14)	0.0024 (15)	−0.0081 (14)	−0.0204 (14)
C11	0.0815 (18)	0.0983 (19)	0.0494 (11)	0.0159 (16)	0.0084 (12)	−0.0074 (12)
C38	0.133 (3)	0.0790 (18)	0.136 (3)	0.0499 (19)	0.087 (2)	0.0236 (18)
C41	0.082 (2)	0.0845 (19)	0.125 (2)	−0.0228 (16)	0.0521 (19)	−0.0064 (17)
C37	0.098 (2)	0.100 (2)	0.115 (2)	−0.0312 (18)	0.0588 (19)	−0.0558 (18)
C40	0.101 (2)	0.115 (2)	0.0773 (17)	0.015 (2)	0.0298 (16)	0.0348 (16)

Geometric parameters (Å, º)

O2—C33	1.336 (3)	C18—H18A	0.9700
O2—C34	1.457 (2)	C18—H18B	0.9700
N3—C8	1.308 (2)	C18—C19	1.500 (3)
N3—C14	1.391 (2)	C28—H28	0.9300
N1—C5	1.381 (2)	C28—C29	1.383 (3)
N1—C16	1.382 (2)	C34—H34	0.9800
N1—C20	1.461 (2)	C34—C35	1.507 (3)
N2—C4	1.391 (2)	C34—C42	1.507 (3)
N2—C16	1.309 (3)	C36—C35	1.534 (3)
N4—C8	1.375 (2)	C36—C38	1.530 (4)
N4—C9	1.387 (3)	C36—C37	1.538 (4)
N4—C15	1.450 (3)	C39—C42	1.534 (3)
O1—C33	1.202 (3)	C39—C41	1.530 (4)
O3—N5	1.287 (2)	C39—C40	1.526 (4)
N5—C36	1.478 (3)	C31—H31	0.9300
N5—C39	1.494 (3)	C31—C30	1.377 (3)
C33—C32	1.499 (3)	C15—H15A	0.9600
C5—C4	1.403 (3)	C15—H15B	0.9600
C5—C6	1.389 (2)	C15—H15C	0.9600
C8—C1	1.481 (2)	C19—H19A	0.9600
C24—C25	1.388 (3)	C19—H19B	0.9600
C24—C23	1.401 (2)	C19—H19C	0.9600
C24—C27	1.494 (2)	C10—H10	0.9300
C21—C22	1.388 (2)	C10—C11	1.377 (4)
C21—C26	1.385 (3)	C35—H35A	0.9700
C21—C20	1.514 (2)	C35—H35B	0.9700
C4—C3	1.401 (3)	C29—H29	0.9300
C3—C2	1.387 (3)	C29—C30	1.374 (4)
C3—C7	1.508 (3)	C7—H7A	0.9600
C16—C17	1.493 (3)	C7—H7B	0.9600

C32—C27	1.398 (2)	C7—H7C	0.9600
C32—C31	1.393 (3)	C13—H13	0.9300
C22—H22	0.9300	C13—C12	1.380 (4)
C22—C23	1.381 (2)	C42—H42A	0.9700
C26—H26	0.9300	C42—H42B	0.9700
C26—C25	1.390 (3)	C30—H30	0.9300
C25—H25	0.9300	C12—H12	0.9300
C1—C2	1.413 (3)	C12—C11	1.391 (5)
C1—C6	1.386 (3)	C11—H11	0.9300
C20—H20A	0.9700	C38—H38A	0.9600
C20—H20B	0.9700	C38—H38B	0.9600
C2—H2	0.9300	C38—H38C	0.9600
C9—C14	1.391 (3)	C41—H41A	0.9600
C9—C10	1.395 (3)	C41—H41B	0.9600
C23—H23	0.9300	C41—H41C	0.9600
C6—H6	0.9300	C37—H37A	0.9600
C14—C13	1.389 (3)	C37—H37B	0.9600
C27—C28	1.393 (3)	C37—H37C	0.9600
C17—H17A	0.9700	C40—H40A	0.9600
C17—H17B	0.9700	C40—H40B	0.9600
C17—C18	1.524 (3)	C40—H40C	0.9600

C33—O2—C34	116.94 (15)	O2—C34—C42	106.74 (16)
C8—N3—C14	104.61 (15)	C35—C34—H34	109.9
C5—N1—C16	106.62 (16)	C35—C34—C42	109.22 (19)
C5—N1—C20	123.67 (15)	C42—C34—H34	109.9
C16—N1—C20	129.52 (16)	N5—C36—C35	110.32 (18)
C16—N2—C4	105.36 (15)	N5—C36—C38	107.6 (2)
C8—N4—C9	105.97 (15)	N5—C36—C37	108.6 (2)
C8—N4—C15	128.04 (16)	C35—C36—C37	111.0 (2)
C9—N4—C15	125.92 (16)	C38—C36—C35	109.1 (2)
O3—N5—C36	115.85 (19)	C38—C36—C37	110.2 (3)
O3—N5—C39	115.63 (19)	N5—C39—C42	110.24 (17)
C36—N5—C39	125.24 (17)	N5—C39—C41	107.1 (2)
O2—C33—C32	112.39 (17)	N5—C39—C40	109.4 (2)
O1—C33—O2	124.1 (2)	C41—C39—C42	109.0 (2)
O1—C33—C32	123.5 (2)	C40—C39—C42	111.5 (2)
N1—C5—C4	105.32 (15)	C40—C39—C41	109.5 (3)
N1—C5—C6	131.47 (17)	C32—C31—H31	119.5
C6—C5—C4	123.22 (17)	C30—C31—C32	121.0 (2)
N3—C8—N4	113.58 (16)	C30—C31—H31	119.5
N3—C8—C1	123.86 (15)	N4—C15—H15A	109.5
N4—C8—C1	122.51 (16)	N4—C15—H15B	109.5
C25—C24—C23	117.72 (16)	N4—C15—H15C	109.5
C25—C24—C27	120.84 (15)	H15A—C15—H15B	109.5
C23—C24—C27	121.25 (15)	H15A—C15—H15C	109.5
C22—C21—C20	121.05 (15)	H15B—C15—H15C	109.5
C26—C21—C22	118.31 (16)	C18—C19—H19A	109.5

C26—C21—C20	120.56 (15)	C18—C19—H19B	109.5
N2—C4—C5	109.89 (17)	C18—C19—H19C	109.5
N2—C4—C3	129.81 (17)	H19A—C19—H19B	109.5
C3—C4—C5	120.29 (16)	H19A—C19—H19C	109.5
C4—C3—C7	120.83 (18)	H19B—C19—H19C	109.5
C2—C3—C4	116.89 (17)	C9—C10—H10	122.0
C2—C3—C7	122.3 (2)	C11—C10—C9	116.0 (2)
N1—C16—C17	122.65 (18)	C11—C10—H10	122.0
N2—C16—N1	112.81 (17)	C34—C35—C36	111.74 (18)
N2—C16—C17	124.46 (17)	C34—C35—H35A	109.3
C27—C32—C33	124.36 (17)	C34—C35—H35B	109.3
C31—C32—C33	115.83 (17)	C36—C35—H35A	109.3
C31—C32—C27	119.80 (19)	C36—C35—H35B	109.3
C21—C22—H22	119.4	H35A—C35—H35B	107.9
C23—C22—C21	121.23 (15)	C28—C29—H29	120.4
C23—C22—H22	119.4	C30—C29—C28	119.3 (2)
C21—C26—H26	119.7	C30—C29—H29	120.4
C21—C26—C25	120.66 (16)	C3—C7—H7A	109.5
C25—C26—H26	119.7	C3—C7—H7B	109.5
C24—C25—C26	121.28 (16)	C3—C7—H7C	109.5
C24—C25—H25	119.4	H7A—C7—H7B	109.5
C26—C25—H25	119.4	H7A—C7—H7C	109.5
C2—C1—C8	117.47 (17)	H7B—C7—H7C	109.5
C6—C1—C8	121.08 (16)	C14—C13—H13	121.2
C6—C1—C2	121.43 (16)	C12—C13—C14	117.6 (3)
N1—C20—C21	112.71 (14)	C12—C13—H13	121.2
N1—C20—H20A	109.1	C34—C42—C39	112.48 (18)
N1—C20—H20B	109.1	C34—C42—H42A	109.1
C21—C20—H20A	109.1	C34—C42—H42B	109.1
C21—C20—H20B	109.1	C39—C42—H42A	109.1
H20A—C20—H20B	107.8	C39—C42—H42B	109.1
C3—C2—C1	122.00 (18)	H42A—C42—H42B	107.8
C3—C2—H2	119.0	C31—C30—H30	120.1
C1—C2—H2	119.0	C29—C30—C31	119.9 (2)
N4—C9—C14	105.46 (16)	C29—C30—H30	120.1
N4—C9—C10	131.8 (2)	C13—C12—H12	119.3
C14—C9—C10	122.7 (2)	C13—C12—C11	121.4 (2)
C24—C23—H23	119.6	C11—C12—H12	119.3
C22—C23—C24	120.76 (16)	C10—C11—C12	122.1 (2)
C22—C23—H23	119.6	C10—C11—H11	119.0
C5—C6—H6	121.9	C12—C11—H11	119.0
C1—C6—C5	116.17 (16)	C36—C38—H38A	109.5
C1—C6—H6	121.9	C36—C38—H38B	109.5
N3—C14—C9	110.37 (17)	C36—C38—H38C	109.5
C13—C14—N3	129.4 (2)	H38A—C38—H38B	109.5
C13—C14—C9	120.1 (2)	H38A—C38—H38C	109.5
C32—C27—C24	124.34 (16)	H38B—C38—H38C	109.5
C28—C27—C24	117.82 (16)	C39—C41—H41A	109.5

C28—C27—C32	117.60 (17)	C39—C41—H41B	109.5
C16—C17—H17A	108.9	C39—C41—H41C	109.5
C16—C17—H17B	108.9	H41A—C41—H41B	109.5
C16—C17—C18	113.36 (17)	H41A—C41—H41C	109.5
H17A—C17—H17B	107.7	H41B—C41—H41C	109.5
C18—C17—H17A	108.9	C36—C37—H37A	109.5
C18—C17—H17B	108.9	C36—C37—H37B	109.5
C17—C18—H18A	108.8	C36—C37—H37C	109.5
C17—C18—H18B	108.8	H37A—C37—H37B	109.5
H18A—C18—H18B	107.7	H37A—C37—H37C	109.5
C19—C18—C17	113.7 (2)	H37B—C37—H37C	109.5
C19—C18—H18A	108.8	C39—C40—H40A	109.5
C19—C18—H18B	108.8	C39—C40—H40B	109.5
C27—C28—H28	118.9	C39—C40—H40C	109.5
C29—C28—C27	122.24 (19)	H40A—C40—H40B	109.5
C29—C28—H28	118.9	H40A—C40—H40C	109.5
O2—C34—H34	109.9	H40B—C40—H40C	109.5
O2—C34—C35	111.22 (16)		

O2—C33—C32—C27	−45.4 (3)	C32—C31—C30—C29	−0.6 (4)
O2—C33—C32—C31	135.0 (2)	C22—C21—C26—C25	1.0 (3)
O2—C34—C35—C36	−179.36 (19)	C22—C21—C20—N1	61.5 (2)
O2—C34—C42—C39	177.69 (18)	C26—C21—C22—C23	−2.3 (3)
N3—C8—C1—C2	−53.7 (2)	C26—C21—C20—N1	−121.76 (19)
N3—C8—C1—C6	124.8 (2)	C25—C24—C23—C22	0.2 (3)
N3—C14—C13—C12	177.2 (2)	C25—C24—C27—C32	149.3 (2)
N1—C5—C4—N2	0.4 (2)	C25—C24—C27—C28	−36.5 (3)
N1—C5—C4—C3	−178.86 (16)	C20—N1—C5—C4	−176.03 (15)
N1—C5—C6—C1	179.56 (17)	C20—N1—C5—C6	4.4 (3)
N1—C16—C17—C18	−75.7 (2)	C20—N1—C16—N2	175.62 (16)
N2—C4—C3—C2	−179.71 (18)	C20—N1—C16—C17	−7.6 (3)
N2—C4—C3—C7	1.8 (3)	C20—C21—C22—C23	174.53 (17)
N2—C16—C17—C18	100.7 (2)	C20—C21—C26—C25	−175.88 (18)
N4—C8—C1—C2	123.50 (19)	C2—C1—C6—C5	−1.0 (3)
N4—C8—C1—C6	−58.1 (2)	C9—N4—C8—N3	1.1 (2)
N4—C9—C14—N3	0.5 (2)	C9—N4—C8—C1	−176.29 (16)
N4—C9—C14—C13	178.3 (2)	C9—C14—C13—C12	−0.1 (4)
N4—C9—C10—C11	−177.2 (2)	C9—C10—C11—C12	−0.2 (4)
O1—C33—C32—C27	136.9 (2)	C23—C24—C25—C26	−1.5 (3)
O1—C33—C32—C31	−42.6 (3)	C23—C24—C27—C32	−35.9 (3)
O3—N5—C36—C35	−169.2 (2)	C23—C24—C27—C28	138.3 (2)
O3—N5—C36—C38	−50.3 (3)	C6—C5—C4—N2	−179.96 (16)
O3—N5—C36—C37	69.0 (3)	C6—C5—C4—C3	0.8 (3)
O3—N5—C39—C42	170.4 (2)	C6—C1—C2—C3	1.2 (3)
O3—N5—C39—C41	52.0 (3)	C14—N3—C8—N4	−0.8 (2)
O3—N5—C39—C40	−66.6 (3)	C14—N3—C8—C1	176.60 (17)
N5—C36—C35—C34	−46.2 (3)	C14—C9—C10—C11	−1.4 (3)
N5—C39—C42—C34	43.7 (3)	C14—C13—C12—C11	−1.5 (4)

C33—O2—C34—C35	83.9 (2)	C27—C24—C25—C26	173.43 (19)
C33—O2—C34—C42	−157.05 (17)	C27—C24—C23—C22	−174.73 (17)
C33—C32—C27—C24	−9.9 (3)	C27—C32—C31—C30	4.2 (4)
C33—C32—C27—C28	175.9 (2)	C27—C28—C29—C30	2.1 (4)
C33—C32—C31—C30	−176.2 (2)	C28—C29—C30—C31	−2.6 (4)
C5—N1—C16—N2	0.5 (2)	C34—O2—C33—O1	−10.3 (3)
C5—N1—C16—C17	177.25 (16)	C34—O2—C33—C32	172.01 (15)
C5—N1—C20—C21	70.0 (2)	C36—N5—C39—C42	−31.0 (3)
C5—C4—C3—C2	−0.6 (3)	C36—N5—C39—C41	−149.4 (2)
C5—C4—C3—C7	−179.1 (2)	C36—N5—C39—C40	92.0 (3)
C8—N3—C14—C9	0.1 (2)	C39—N5—C36—C35	32.3 (3)
C8—N3—C14—C13	−177.4 (2)	C39—N5—C36—C38	151.2 (2)
C8—N4—C9—C14	−0.96 (19)	C39—N5—C36—C37	−89.6 (3)
C8—N4—C9—C10	175.4 (2)	C31—C32—C27—C24	169.7 (2)
C8—C1—C2—C3	179.62 (16)	C31—C32—C27—C28	−4.5 (3)
C8—C1—C6—C5	−179.37 (15)	C15—N4—C8—N3	178.2 (2)
C24—C27—C28—C29	−173.2 (2)	C15—N4—C8—C1	0.8 (3)
C21—C22—C23—C24	1.7 (3)	C15—N4—C9—C14	−178.1 (2)
C21—C26—C25—C24	1.0 (3)	C15—N4—C9—C10	−1.8 (4)
C4—N2—C16—N1	−0.2 (2)	C10—C9—C14—N3	−176.19 (19)
C4—N2—C16—C17	−176.91 (17)	C10—C9—C14—C13	1.6 (3)
C4—C5—C6—C1	0.1 (3)	C35—C34—C42—C39	−62.0 (2)
C4—C3—C2—C1	−0.4 (3)	C7—C3—C2—C1	178.1 (2)
C16—N1—C5—C4	−0.53 (18)	C13—C12—C11—C10	1.7 (5)
C16—N1—C5—C6	179.91 (18)	C42—C34—C35—C36	63.1 (3)
C16—N1—C20—C21	−104.4 (2)	C38—C36—C35—C34	−164.2 (3)
C16—N2—C4—C5	−0.2 (2)	C41—C39—C42—C34	161.0 (2)
C16—N2—C4—C3	179.05 (19)	C37—C36—C35—C34	74.2 (3)
C16—C17—C18—C19	−179.7 (2)	C40—C39—C42—C34	−78.1 (3)
C32—C27—C28—C29	1.4 (3)		